Numerical prediction of ac electro-osmotic flows around polarized electrodes

Y. K. Suh* and S. Kang
Department of Mechanical Engineering, Dong-A University, 840 Hadan-dong, Saha-gu, Busan 604-714, Korea
(Received 26 August 2008; revised manuscript received 24 November 2008; published 7 April 2009)

In this paper we present an interactive numerical method that can predict ac electro-osmotic flows around completely polarized electrodes. In this method the slip velocity on the electrode surface is calculated by numerically solving the Laplace equation for the potential in the bulk coupled with the dynamical equation for the surface charge density on the electrodes; here the dynamical equation has been derived from the asymptotic solutions of the Poisson-Nernst-Planck equation for the potential drop across the electrical thin layer near the electrode. A unique feature of this study is that the effect of nonspecific ion adsorption is considered. The numerical code was applied to the two-dimensional ac electro-osmotic flow above a pair of coplanar electrodes, and the solutions compared well with the experimental data reported in the literature. We investigated the effect of various parameters on the slip velocity distribution, such as the ac frequency, the electrode length, the effective Stern-layer thickness, and the adsorption coefficients.

DOI: 10.1103/PhysRevE.79.046309 PACS number(s): 47.61.Fg, 47.57.jd

I. INTRODUCTION

Consider a confined space filled with a liquid solution with cations and anions. When an ac potential is applied to a pair of coplanar electrodes patterned on the boundary surface, both ions are alternately attracted to and repelled from the electrode surfaces giving rise to nonzero charge distribution within electrical thin layers, called the Debye layer or more precisely the inner layer (refer to Suh and Kang [1] for the term "inner layer"). This modifies the electric field and brings nonzero tangential component of the field in the layers. Since both the charge and electric field change their signs simultaneously during one period of ac, the time average of the electric force exerted on each of the ions is nonzero. Then the surrounding fluid is dragged by the viscous action yielding a steady flow around the electrodes, which is called the ac electro-osmotic flow.

Recently, increased attention has been given to the application of the concept of ac electro-osmotic flows to pumping of liquid in microfluidics. The primary element for fluid pumping is composed of a pair of asymmetric electrodes. Ajdari [2] first suggested using asymmetric electrode arrays in pumping liquids in microscales and addressed many possible configurations of electrode arrays for enhancement of pumping speed. Later, Brown *et al.* [3] presented slip-velocity data measured above an array of asymmetric pairs of electrodes for pumping water. They stressed that to improve their simple model various effects must be combined such as the Stern-layer effect and ion motion within double layers etc. Studer *et al.* [4,5] reported fabrication of an integrated pumping system utilizing ac electro-osmosis and investigated the performance as well as feasibility of their system for use as an element in a lab-on-a-chip device. The measured pumping speed reached up to 500 μm/s with only a few volts, and interestingly enough they observed reversal flows. Mpholo *et al.* [6] showed that by placing two anisotropic arrays of indium tin oxide electrodes in a channel they can attain the pumping velocity as much as 450 μm/s. Olsen *et al.* [7] extended the existing theory in order to study the effect of the confinement of the channel geometry and the Faradaic injection for ac electro-osmotic pumping. Brask *et al.* [8] reported an ac electro-osmotic pump supplemented by bubble-free palladium and rectifying polymer membrane valves. The electrode pair used for the pumping need not necessarily be coplanar. The Bazant group [9–11] demonstrated that nonplanar structure of the electrode pairs indeed provided faster flows.

Application of the ac electro-osmotic phenomenon to microfluidics requires development of theoretical models that can predict the slip velocity on the electrode walls with reasonable accuracy but should be as simple as possible. In microscales, Debye layers are so thin compared with the other geometrical size that doing numerical simulation for the full ion transport equations, i.e., the Nernst-Planck (NP) equation, together with the Poisson equation for the potential over the whole domain including the Debye layers is not efficient. Therefore appropriate modeling of the ion transport within the layers is demanded. Gonzalez *et al.* [12] proposed a simple capacitor model to verify the magnitude of the slip velocity measured on the coplanar electrode pair. However, the predicted velocity turned out to be much greater than the measured one. Later, Green *et al.* [13] refined their capacitor model by introducing the effect of potential drop across the compact (Stern) layer. They could predict their measured data with fairly good accuracy but in doing so they had to employ a nonlinear impedance-frequency relationship obtainable through experiments. Application of the ac electro-osmosis to the DNA concentration has been tried by Brown and Meinhart [14] with the electrode arrangement very similar to that used by Wong *et al.* [15], and they revealed that the numerical results were two orders of magnitude greater than the measured ones. Further, the predicted critical frequency, at which the slip velocity becomes maximum, was also more than two orders of magnitude smaller than the experimental data. The contribution of the Bazant group [16–19] focused on the transient process of the ion transport under the different name 'induced-charge electro-osmosis' for the similar phenomenon. Their capacitor model also

*Corresponding author. FAX: 82-51-200-7656. yksuh@dau.ac.kr

showed deviation from the experimental observation.

Very recently Suh and Kang [1] showed that under ac electric field the electric layer must be of a triple-layer structure composed of the Stern layer, inner layer (usually called diffuse layer), and middle layer. They have demonstrated that ion depletion can happen in the middle layer at high external potentials corresponding to a strongly nonlinear regime, which is the primary reason for the breakdown of the weakly nonlinear model. They have also proposed an interactive numerical scheme for solving the Laplace equation for the bulk potential coupled by a dynamic equation representing the evolution of the surface charge on the electrodes. They applied their interactive numerical method to the one-dimensional problem for the ion transport in between a pair of facing electrodes and the results were proved to be in excellent agreement with those given by the full equations. They have finally proposed to include an ion-adsorption model in the dynamic equation for the surface charge that was proven to reduce the magnitude of the slip velocity as much as needed without affecting the critical frequency as much.

In this paper we apply our model proposed in [1] relevant for weakly nonlinear cases to the two-dimensional problem of ac electro-osmosis above a pair of coplanar symmetric electrodes. The purpose of this study is to confirm the validity of our model by applying it to a two-dimensional (2D) model flow and comparing the numerical results with the experimental data presented by Green *et al.* [13].

In the following section, we present the governing equations, derivation of the slip velocity, and details of the numerical methods. The numerical results are then presented and discussed in Sec. III. Important parameters involved in the numerical simulation are addressed in the first part of this section. The main code is developed based on the transformed coordinates so that very fine grids can be built near the leading edge of the electrodes. The developed code is validated by comparing the results obtained with different grid resolutions and also by comparing the results with the ones given by the code developed with the Cartesian coordinates. We next investigate the effect of various parameters including the ac frequency, the electrode length as well as the domain size, the effective Stern-layer thickness, and the adsorption, etc. Then, we demonstrate the successful matching of our numerical slip velocity with the data reported by Green *et al.* [13] for two kinds of electrolytes. In the last part of Sec. III, further discussion is given to the numerical results of a strongly nonlinear case and the symptom of the breakdown of the weakly nonlinear model. Finally, our conclusion is summarized in Sec. IV.

II. GOVERNING EQUATIONS AND NUMERICAL METHODS

A. Governing equations

The domain of interest under consideration is assumed to be occupied by a dilute monovalent symmetrical electrolyte ($z^+=-z^-=1$) with each ion's bulk concentration c_0^* (number density). For further simplicity, we confine ourselves to a two-dimensional problem in this paper. Extension to a three-dimensional domain with multivalent asymmetric electrolyte should be straightforward. Figure 1(a) illustrates, as an example of the model problem treated in this study, the 2D space above the bottom wall on which a pair of planar electrodes are built. As usual, we assume completely polarized electrodes so that no faradic current flows across the electrode surfaces. We denote the Cartesian coordinate system $\mathbf{x}^*=(x^*,y^*)$ and the velocity vector $\mathbf{u}^*=(u^*,v^*)$. In the following, the variables with " *" as the superscript in general represent the dimensional quantities and the ones without " *" the dimensionless ones. However, for those parameters denoted by widely used symbols for which we do not separately need to define the corresponding dimensionless quantities, we will use the bare symbols, without " *," as the dimensional quantities.

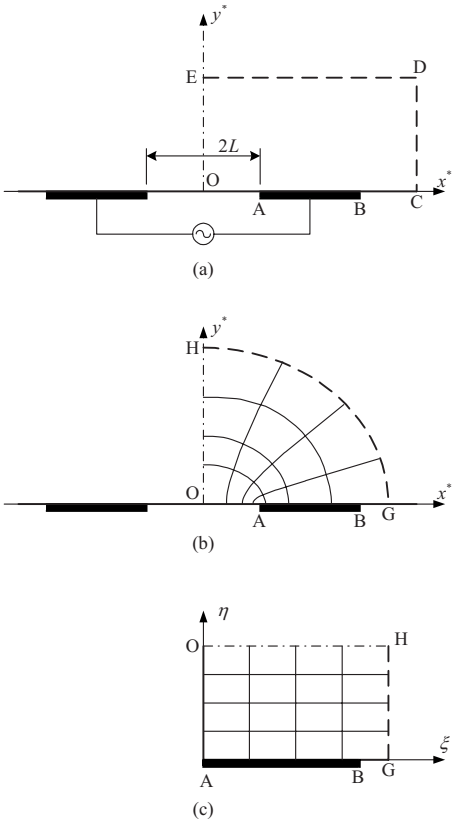

FIG. 1. Two-dimensional space for numerical simulation of the electro-osmotic flows around a pair of coplanar electrodes (indicated by a horizontal bar A-B on the bottom wall); (a) physical space to be treated by the Cartesian coordinates (x^*,y^*) with the rectangular boundary O-C-D-E; (b) physical space to be treated by curvilinear coordinates with the curved outer boundary G-H; (c) transformed space defined by the coordinates (ξ,η) constructed by a conformal mapping. Notice the clustering of grids near the electrode edge A in (b).

The electro-osmotic flow of the incompressible fluid around the pair of electrodes is governed by the following equations:

$$\nabla^* \cdot \mathbf{u}^* = 0, \tag{1a}$$

$$\rho^* \frac{\partial \mathbf{u}^*}{\partial t^*} = -\nabla^* p^* + \mu \nabla^{*2} \mathbf{u}^* - \rho_e^* \nabla^* \phi^*, \tag{1b}$$

where t^* is the time, p^* is the pressure, ϕ^* is the electric potential, ρ^* is the fluid density, μ is the fluid viscosity, and ∇^* is the gradient operator. Here the nonlinear convective terms have been neglected as is usually true in microfluidics. To solve the above equations, we need to impose boundary conditions for the velocity components. At this time we must apply the no-slip and impermeable boundary conditions all over the surrounding boundaries including the electrode walls. In Eq. (1b), ρ_e^* is the charge density (charge per unit volume) given by

$$\rho_e^* = (c^{*+} - c^{*-})e. \tag{2}$$

Here, $c^{*\pm}$ denotes the concentration of the cation and anion, respectively, and $e = 1.602 \times 10^{-10}$ C is the electron charge. The last term on the right-hand side (RHS) of Eq. (1b) is the only body force that drives the viscous fluid flow. This force vanishes in the bulk because it is neutralized, i.e., $c^{*+} \approx c^{*-} \approx c_0^*$ and $\rho_e^* \approx 0$ there. Except for the strongly nonlinear case, the middle layer is also neutralized. Within the inner layer, however, non-neutralized distribution of the ions leads to a nonzero value of ρ_e^*.

Ion concentrations are determined from the Nernst-Planck equation [1],

$$\frac{\partial c^{*\pm}}{\partial t^*} = \nabla^* \cdot \left[D \nabla^* c^{*\pm} \pm D \left(\frac{e}{k_b T} \right) c^{\pm} \nabla^* \phi^* \right], \tag{3}$$

where D is the diffusivity of ions, k_b is the Boltzmann constant, and T is the temperature. Here again the nonlinear convective terms have been neglected under plausible assumptions. The first and second terms within the square brackets on the RHS of Eq. (3) represent the diffusion effect and the conduction (or ion migration) one, respectively. The electric potential is intrigued by the presence of the charge distribution and is calculated from the Poisson equation,

$$\nabla^* \cdot (\varepsilon \varepsilon_0 \nabla^* \phi^*) = -\rho_e^*. \tag{4}$$

Here, $\varepsilon_0 = 8.85 \times 10^{-12}$ C/V m is the dielectric permittivity of the vacuum and ε is the relative permittivity of the fluid. The boundary conditions for Eq. (4) are $\partial \phi^* / \partial n^* = 0$ on the surface of the nonconducting walls, where n^* represents the dimensional local coordinate normal to the wall, and $\phi^* = \pm V_{00}^* \cos \omega t^*$ on the left-hand side (LHS) and RHS electrode surfaces, respectively. Here, V_{00}^* is the peak-to-peak amplitude of the external ac potential applied on the electrodes and ω is its angular frequency. Since the convection effect has been neglected, the system of equations that determine the electrochemical variables $c^{*\pm}$, ρ_e^*, and ϕ^*, i.e., Eqs. (2)–(4), are decoupled from the hydrodynamic equations, namely Eqs. (1a) and (1b).

Associated with the solutions of Eqs. (3) and (4), we have two important length scales; see Suh and Kang [1]. The first one is the Debye length defined as

$$\lambda_d = \sqrt{\frac{\varepsilon \varepsilon_0 k_b T}{2 e^2 c_0^*}}, \tag{5}$$

which represents the order of the inner-layer thickness. This length comes from the balance between the diffusion and conduction terms in Eq. (3) while neglecting the LHS term. This means that the inner layer is characterized by a quasisteady state. Of course this quasisteady state can be feasible only when the ac frequency is not so high; as a practical guide, the frequency below 10 kHz will be enough for such a state to be observable. In other words, if the external ac period is much longer than the charging time, which is usually very short, we can expect the inner layer. The second length scale comes from the balance between the LHS transient and diffusion terms in Eq. (3) reading

$$\lambda_{\mathrm{dif}} = \sqrt{\frac{D}{\omega}}, \tag{6}$$

which represents the thickness of the middle layer. The middle layer is usually much thicker than the inner layer if ω is not so large and much thinner than the bulk scale if ω is not so small; indeed this is the case in various practical applications of ac electro-osmosis in microfluidics.

According to the analysis of Suh and Kang [1], cations and anions in the inner layer respond to the external ac field spontaneously but show alternately different accumulation of ions during one ac period, $2\pi/\omega$. Contrary to this, both ions in the middle layer show the same behavior with each other for the weakly nonlinear case. Therefore the nonzero potential drop occurs only across the inner layer, which is very thin in terms of the bulk scale. So, from this fact together with the fact that the hydrodynamic equations are decoupled from the other ones, we are allowed to delete the last term in Eq. (1b) but instead change the boundary condition on the electrode walls from the no-slip to the slip type with an appropriate slip velocity. Calculation of this slip velocity always becomes the primary part of the whole numerical-simulation procedure for electro-osmotic flows.

Calculation of the ac electro-osmotic flow field is performed in general by two steps. In the first step, the unsteady slip velocity at the outer edge of the electrical thin layers is obtained from the interactive numerical simulation of the Laplace equation for the potential in the bulk including the middle layer and the dynamical equation for the surface charge density on the interface between the Stern and inner layers. Then the steady slip velocity is calculated from time average of the unsteady velocity data over one ac period. In the second step, the hydrodynamic equations (1a) and (1b), the last term being omitted in Eq. (1b), are solved by using the steady slip velocity obtained in the first step as the boundary condition specified on the electrode surfaces. In this paper, we are interested mainly in the first step, because the second step is not so much involved as the first one.

B. Slip velocity

The detailed derivation of the formula needed to obtain the slip velocity has been given in Suh and Kang [1]. In this paper, we just present important formulas. First we need to

make the variables dimensionless as follows: $\mathbf{x}^*=L\mathbf{x}$, $t^*=t/\omega$, $c^{*\pm}=c_0^*c^{\pm}$, $\phi^*=\phi_{\text{ref}}^*\phi$, and $\rho_e^*=c_0^*e\rho_e$, where L is the reference length such as half the distance between the pair of electrodes as shown in Fig. 1(a), $\phi_{\text{ref}}^*=(L/\lambda_d)^2(D/L^2\omega)\varsigma^*/2$ is the reference potential, and $\varsigma^*=k_bT/e$ is the thermal potential. In this formulation we assume that D, ε, and T remain constant.

The thickness of the Stern and inner layers is usually of O (nm) being much smaller than the size of fluidic devices we are interested in. So, we separate the domain into two parts; the neutralized bulk and the middle layer (referred to as "outer layer" hereafter) where the charge density is zero and the thin region composed of the Stern and inner layers (referred to as "inner region" hereafter) where a substantial amount of potential drop takes place due to the nonzero charge density. The induced dimensionless potential, $\phi(\mathbf{x},t)$, in the outer region is governed by the Laplace equation,

$$\nabla^2\phi=0. \tag{7}$$

This is valid when, first, the region is electrically neutralized and, second, the concentrations are uniformly distributed; see, e.g., [19,20] for the detailed discussion on this issue. In the bulk region both requirements are satisfied as far as the Debye length remains thin enough. We will see in this paper that in the middle layer they are also approximately satisfied for the weakly nonlinear cases but not for the strongly nonlinear cases. Since the inner region is very thin we neglect it in defining the computational domain for solving Eq. (7). The boundary condition at the surface of nonconducting walls [i.e., O-A and B-C-D-E in Fig. 1(a) and O-A and B-G-H in Fig. 1(c)] are set at $\partial\phi/\partial n=0$, and along the symmetric line [i.e., O-E in Fig. 1(a) and O-H in Fig. 1(c)] we set at $\phi=0$. In order to provide the boundary condition on the electrode surface (more precisely at the outer edge of the inner layer), we must consider the effect of the potential drop across the Stern and inner layers.

The dimensionless potential at the edge of the inner layer is determined from

$$\phi_w(s,t)=V_{00}\cos t-\Delta\phi_S-\Delta\phi_i, \tag{8}$$

where $\Delta\phi_S(s,t)$ and $\Delta\phi_i(s,t)$ indicate the potential drops across the Stern and inner layers, respectively. Here, the coordinate s denotes the dimensionless distance of a point on the electrode surface measured from a particular point such as the leading edge of the electrode for the coplanar case. The asymptotic analysis of Suh and Kang [1] for the inner region provided the following formula:

$$\Delta\phi_S=-\varepsilon_2(q+\sigma_a), \tag{9a}$$

$$\Delta\phi_i=-\frac{1}{\gamma}\ln\left(\frac{\sqrt{16/\gamma+q^2}+q}{\sqrt{16/\gamma+q^2}-q}\right). \tag{9b}$$

In the above equations, q is the dimensionless surface charge density representing the effect of the charge accumulation in the inner layer, and σ_a is the dimensionless surface charge density caused by the ion adsorption at the interface between the Stern and inner layers; detailed formula for q and σ_a will be presented shortly. Parameters ε_2 and γ in Eqs. (9a) and (9b) are defined as follows:

$$\varepsilon_2=\frac{\lambda_{\text{Seff}}}{\sqrt{2}\varepsilon_1 L},$$

$$\gamma=\phi_{\text{ref}}^*/\varsigma^*=\frac{1}{2}(L/\lambda_d)^2\varepsilon_1^2,$$

where ε_1 is a small parameter defined as

$$\varepsilon_1=\sqrt{D/L^2\omega}=\lambda_{\text{Seff}}/L,$$

and λ_{Seff}, the effective thickness of the Stern layer, is related to the actual Stern layer thickness λ_S as follows:

$$\lambda_{\text{Seff}}=\lambda_S\varepsilon/\varepsilon_S, \tag{10}$$

where ε_S is the dielectric constant of the medium in the Stern layer.

The surface charge density $q(s,t)$ used in Eqs. (9a) and (9b) is determined from the dynamical equation [1]

$$\frac{\partial q}{\partial t}=\frac{2\sqrt{2}\varepsilon_1\gamma}{1+\beta}\left(\frac{\partial\phi}{\partial n}\right)_w, \tag{11}$$

where the subscript "w" indicates that the corresponding quantity should be evaluated at the electrode wall from the solution of the Laplace equation for the outer region; the subscript is also used in the analysis of the inner layer, i.e., Eq. (8), as the outer edge of the layer based on the fact that the outer limit of the inner layer must be matched with the inner limit of the outer region, the bulk. In the above equation, the variable $\beta(s,t)$ denotes the effect of the ion adsorption:

$$\beta=\frac{8\Gamma_{\max}\alpha\sqrt{\gamma}(8+16\alpha+\gamma q^2)}{\sqrt{16+\gamma q^2}(4+8\alpha+\alpha\gamma q^2)}. \tag{12}$$

Here parameters $\Gamma_{\max}$ and α are made dimensionless from the corresponding dimensional quantities $\Gamma_{\max}^*$ and α^* as follows:

$$\Gamma_{\max}=\frac{\sqrt{2}\Gamma_{\max}^*}{c_0^*\lambda_{\text{dif}}},\quad \alpha=c_0^*\alpha^*. \tag{13}$$

We note that the formula (12) has been derived based on the Langmuir-type isotherm [1]

$$\Gamma^{\pm}=\frac{\Gamma_{\max}\alpha c^{\pm}}{1+\alpha(c^+ + c^-)}. \tag{14}$$

On the other hand, the surface charge density $\sigma_a(s,t)$ in Eq. (9a) representing the ion adsorption at the interface is to be calculated from

$$\sigma_a=\frac{\Gamma_{\max}\alpha\gamma q\sqrt{16/\gamma+q^2}}{4+8\alpha+\alpha\gamma q^2}. \tag{15}$$

As introduced in Suh and Kang [1], $\Gamma_{\max}^*$ represents the maximum limit of the permissible number of ions per unit area adsorbed at the electrode surface. We can roughly estimate this magnitude by the formula, $\Gamma_{\max}^*\approx 1/A^*$, where A^*

TABLE I. Two types of KCl solution used in the present numerical study.

Type	κ (S/m)	c_M^* (mole/l)	c_0^* (m^{-3})	D (m^2/s)	λ_d (nm)
A	0.0021	0.141×10^{-3}	0.850×10^{23}	1.92×10^{-9}	25.4
B	0.0086	0.583×10^{-3}	3.51×10^{23}	1.90×10^{-9}	12.5

denotes the minimum area available for allowing one ion to be adsorbed on the surface. Suppose that every adsorbed ion is spread on the electrode surface in a hexagonal shape, then we can compute A^* from

$$A^* = 2\sqrt{3}a^{*2}, \tag{16}$$

where $2a^*$ is the side length of the hexagon. Further, we assume that a^* corresponds to the ionic radius, which can be obtained from the formula of the mobility,

$$m = \frac{F}{6\pi a^* \mu N_A}, \tag{17}$$

where $N_A=6.02\times10^{23}$ is the Avogadro number. Using the numerical values $m=7.6\times10^{-8}$ and 7.9×10^{-8} $m^2\,\Omega/V$ for the K^+ and Cl^- ions, respectively, we can derive $a^*=0.112$ and 0.108 nm for each ion. Assuming again that both ions have the same ionic radius, $a^*=0.11$ nm, we arrive at $\Gamma_{\max}^* \approx 2.39\times10^{19}$ m^{-2}. But this should be considered only as a reference value. There must be several factors to be addressed before presenting a physically plausible value of $\Gamma_{\max}^*$. First, the mobility formula (17) is derived under a dilute-solution condition, and for the case of high concentrations it must be modified. Second, but more importantly, the minimum area one ion can take with highest population, i.e., A^*, may be more involved than the simple form like (16). Third, the affinity between the electrode and the electrolyte may also affect the value of A^*.

The physical meaning of the parameter α^* can be understood from the formula (14). It shows that when either c^+ or c^- approaches infinity, the magnitude of Γ^+ or Γ^- becomes saturated to $\Gamma_{\max}$. For instance, Γ^+ reaches approximately 90% of $\Gamma_{\max}$ at $c^+=9\alpha^{-1}$; in the dimensional quantities, we may say that the interface is saturated with 90% coverage of the adsorbed cations when the cation concentration at the interface reaches $c^{*+}=9/\alpha^*$. Therefore α^* should plausibly take the numerical value in the order of $1/c_0^*$. As a typical example, for the electrolyte type A of KCl shown in Table I, we have $1/c_0^*=1.2\times10^{-23}$ m^3. In this paper we will tune the two parameters $\Gamma_{\max}^*$ and α^* (or sometimes their dimensionless quantities) and see in what extent they can reproduce the experimental data.

The dimensional "instantaneous" slip velocity $u_s^*(s,t)$ at the outer edge of the inner layer (or at the electrode wall viewed from the outer region) caused both by the potential drop across the inner layer and by the tangential gradient of the potential is given by

$$u_s^* = \left(\frac{\varepsilon\varepsilon_0}{\mu L}\phi_{\text{ref}}^{*2}\right)\Delta\phi_i\frac{\partial\phi_w}{\partial s}. \tag{18}$$

In deriving this formula the adsorbed ions are assumed to be immobile and thus do not contribute to the slip velocity. The steady-state slip velocity $u_{\text{slip}}^*(s)$ is then obtained from the time average of the instantaneous quantity; $u_{\text{slip}}^*=\langle u_s^*\rangle$.

Determining distribution of the slip velocity u_{slip}^* on the electrode surface is the primary goal of the numerical simulation before going to the Navier-Stokes equation for establishing the flow field over the domain. As can be seen from Eq. (18), we need to find both the tangential component of the electric field, $\partial\phi_w/\partial s$, and the potential drop across the inner layer, $\Delta\phi_i$. These are ultimately provided from the solution of the Laplace equation (7).

C. Numerical method and procedure

It is now clear that we must solve the Laplace equation (7) for ϕ in coupling with the dynamic equation (11) for q. In more details, in solving Eq. (7) we need ϕ_w as the boundary condition on the electrode wall and this is determined from q as shown in Eqs. (8), (9a), (9b), and (15). On the other hand, in solving Eq. (11) for q we need the potential gradient $(\partial\phi/\partial n)_w$ and this is determined from the solution of Eq. (7). We employed the finite volume method in solving Eq. (7) by using two different types of grid systems. In solving Eq. (11), a different algorithm has been used depending on the grid system used for the discretization.

The first grid system is made based on the Cartesian coordinates (x,y), and in this case the computational domain is just a rectangle in the physical space, i.e., O-C-D-E in Fig. 1(a). With the uniform grids, Eq. (7) is disctretized by using the central difference formula. The resultant algebraic equations are solved by using the SOR (successive over relaxation) method. From the solution obtained in this way, the potential gradient $(\partial\phi/\partial n)_w$ is computed at each grid point on the electrode surface, which is then used in updating q from Eq. (11) as follows:

$$q^k = q^{k-1} + \Delta t\left[\frac{2\sqrt{2}\varepsilon_1\gamma}{1+\beta}\left(\frac{\partial\phi}{\partial n}\right)_w\right]^{k-1}, \tag{19}$$

where the superscript "k" denotes the time level. The updated q is then applied to Eqs. (15), (9b), and (9a) to ultimately compute ϕ_w^k from Eq. (8). This quantity is again used as the boundary condition on the electrode wall in solving Eq. (7) for ϕ^k, and this completes one cycle of the computation for the time level k. Since the value of ϕ_w needed in solving Eq. (7) and that of $(\partial\phi/\partial n)_w$ needed in solving Eq. (11) are provided explicitly, this method is called the "explicit method."

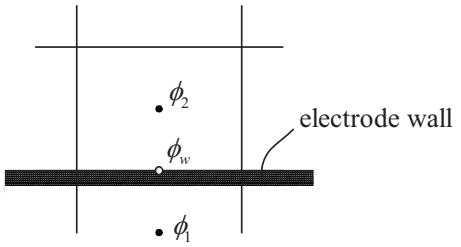

FIG. 2. Computational cell just above the electrode wall and definition points for the three discrete potentials.

Since a high gradient in the potential function is expected near the edges of the electrodes, we need to design clustered grids there for more accurate numerical results. Therefore, to produce the second grid type, we introduce new coordinates (ξ, η) transformed from the Cartesian coordinates with the following conformal mapping:

$$x = \cosh(\pi\xi/2)\cos(\pi\eta/2), \quad y = \sinh(\pi\xi/2)\sin(\pi\eta/2).$$

In the (ξ, η) space, the computational domain is a rectangle as shown in Fig. 1(c) and the outer boundary G-H [dashed line in Fig. 1(c)] maps to a quarter of ellipse in the (x,y) space [dashed line G-H Fig. 1(b)]. We notice the clustering of grids near the leading edge of the electrode as shown in Fig. 1(b). In general, the effect of the detailed geometry of the outer boundaries can be considered to be insignificant as far as they are apart enough from the electrodes, or in more specific terms, when the reference length L remains small compared with the domain size; so, use of the transformed coordinates in the simulation is plausible or even more preferable than the Cartesian coordinates. However, in this grid system, the time step must be taken small because of the numerical instability caused by small grid size near the electrode edge with the explicit method.

To overcome such numerical instability in computation with the transformed grids, we applied an implicit method. First, we take time derivative to Eq. (8),

$$\frac{\partial \phi_w}{\partial t} = H(q)\left(\frac{\partial \phi}{\partial \eta}\right)_w - V_{00}\sin t, \tag{20}$$

where $H(q)$ reads

$$H(q) = 2\sqrt{2}\gamma\varepsilon_1\left(\frac{\partial \eta}{\partial y}\right)_w\left[\varepsilon_2 + \frac{2}{(1+\beta)\gamma\sqrt{16/\gamma + q^2}}\right].$$

Next, we apply the Euler implicit algorithm to Eq. (20) to get

$$\frac{\phi_w^k - \phi_w^{k-1}}{\Delta t} = H^{k-1}\left(\frac{\phi_2^k - \phi_1^k}{\Delta\eta}\right) - V_{00}\sin t, \tag{21}$$

where $H^{k-1}=H(q^{k-1})$, and ϕ_2 and ϕ_1 denote the discrete variables defined at the center of the interior cell just above the electrode wall and at the center of the exterior cell just below the wall (see Fig. 2), respectively. We then replace ϕ_w on the LHS of Eq. (21) with ϕ_2 and ϕ_1 by using the relation $\phi_w = (\phi_1+\phi_2)/2$ to arrive at the formula relating ϕ_1^k and ϕ_2^k as follows:

$$\phi_1^k = \left(\frac{-1 + 2H^{k-1}\Delta t/\Delta\eta}{1 + 2H^{k-1}\Delta t/\Delta\eta}\right)\phi_2^k + \left(\frac{\phi_1^{k-1} + \phi_2^{k-1} - 2\Delta t V_{00}\sin t}{1 + 2H^{k-1}\Delta t/\Delta\eta}\right).$$

Substitute this into the discretized equation of Eq. (7) for the cell just above the electrode wall, having ϕ_2^k as the centered variable, and remove ϕ_1^k to obtain the final form of the algebraic equation for the cell, which is then subjected to the solver SOR. In this algorithm, we further need to know q for given ϕ_w in evaluation of $H(q)$. For this, we solved the nonlinear equation (8) for q by using the Newton-Rhapson method. It was found that a few iterations are enough to obtain the converged value with reasonable accuracy in most cases. We confirmed from sample simulations that the implicit algorithm with the transformed coordinates indeed enhanced the numerical stability significantly.

III. NUMERICAL RESULTS

A. Review of parameters and validation of the code

Before presenting the numerical results, we must review the various parameters involved in this study. We employed, as the electrolyte, two kinds of the KCl solution, i.e., types A and B, used by Green *et al.* [13]. They presented the conductivity κ instead of the concentrations for each of the electrolytes. Table I shows the detailed properties of each type derived in this study. In the table, the number concentrations c_0^* in m^{-3} are computed from $c_0^* = 1000 N_A c_M^*$. For a given κ in S/m, the molar concentration c_M^* in mole/l is obtained by solving the following empirical formula:

$$149.9c_M^* - 94.7(c_M^*)^{1.5} + 91(c_M^*)^2 = 10\kappa,$$

which has been derived from the data of conductivity presented in the literature. On the other hand, the diffusivity of each solution is calculated by using the formula

$$D = \frac{k_b T\kappa}{2e^2 c_0^*}.$$

Following the experimental setup of Green *et al.* [13], we set the gap between the electrode pair at $2L=25$ μm. The temperature is set at $T=288$ K, the viscosity at $\mu = 0.001$ Ns/m^2, and the relative permittivity of the fluid at $\varepsilon=80$. Other parameters varied in this study are the number of grids $I\times J$ or the dimensionless spatial grid size Δx and Δy, the dimensionless time step Δt, the ac frequency f, the amplitude of the external ac potential V_{00}^*, and the effective Stern-layer thickness λ_{Seff}. We also investigated the effect of the domain size by changing x_m, the x coordinate of point C in Fig. 1(a) for the Cartesian coordinate system and that of the point G in Fig. 1(b) for the transformed system, and y_m, the y coordinate of the point E for the Cartesian coordinate system. The effect of the electrode length is also studied by changing x_{em}, i.e., the coordinate of the point B in Figs. 1(a) and 1(b); the actual electrode length L_e is related to x_{em} by $L_e = L(x_{em}-1)$.

In the following we present the numerical results mostly in terms of u_{slip}^* the dimensional slip velocity with the physical unit μm/s. On the other hand, since the experimental

data reported in Green *et al.* [13] were measured at four discrete points on the electrode, say at $s^*=5$, 10, 15, and 20 μm from the leading edge, we must define u_5^*, u_{10}^*, etc., representing the dimensional slip velocity at each of their measurement points discriminated by the subscript.

We validated our code by comparing the slip velocities obtained with different grid resolutions. For $x_m=x_{em}=41$, $V_{00}^*=0.25$ V, $\lambda_{\mathrm{Seff}}=10$ nm, $\Gamma_{\max}^*=5\times10^{16}$ m^{-2}, $\alpha^*=3.16\times10^{-23}$ m^3, and $f=100$ Hz, we conducted the simulation by using the code for the transformed grids with the number of time steps per one period set at $N=2000$; we call this parameter set, except for the frequency, as "standard." The slip velocities u_5^*, u_{10}^*, etc., obtained with the grids $I\times J=41\times21$ were found to keep the same three digits as the corresponding ones obtained with a higher resolution $I\times J=81\times41$. At $f=1000$, difference between the results with $I\times J=41\times21$ and those with $I\times J=81\times41$ is found to be within 1.1%. Therefore in this study we conducted numerical simulations by using the code of transformed grids with $I\times J=81\times41$. Further, our two types of codes are also validated by comparing the results with each other. Of course, the shape of the domain in the two codes differs from each other as explicitly shown in Figs. 1(a) and 1(b). So, direct comparison should have a limited consequence. For $x_m=x_{em}=11$ and all the other parameters set at the standard values, the code with Cartesian grids $I\times J=81\times81$ at $f=100$ Hz underestimates the slip velocity with 2.6% error. This error is decreased down to 1.4% for the grids $I\times J=321\times321$. At $f=1000$ Hz, the error is about 6.5% for $I\times J=81\times81$ and 0.3% for $I\times J=321\times321$. Such amount of errors is assumed to be not problematic in the present study. From this comparison, we can assure that the developed codes are reliable and they should provide solutions accurate enough with a suitable choice of grids. All the numerical results presented in the following sections have been obtained by using the code of transformed grids with the standard parameter set otherwise specified.

B. Typical numerical results, fundamental mechanism, and the frequency effect

Figure 3 shows typical distributions of the dimensional slip velocity u_{slip}^* obtained numerically at three frequencies. It is now well known from numerical as well as experimental studies on the effect of the frequency that there is a critical frequency f_c at which u_{slip}^* becomes maximized. Thus we selected $f=2000$, 250, and 40 Hz as the representative of the supercritical, critical, and subcritical cases, respectively. We can see from Fig. 3 that in a broad range of x, the critical case gives the largest u_{slip}^*. The supercritical case shows confinement of the slip velocity to the leading edge, $x=1$, and a sharp decrease of u_{slip}^* with x. The subcritical case shows distribution of u_{slip}^* in a lower but flatter level than the other cases.

In the remainder of this section, we will address the fundamental mechanism of the slip velocity in terms of the effect of the frequency. Figure 4 shows typical distributions of the potential $\phi(x,y,t)$ in a time sequence during one ac period obtained at a supercritical frequency, $f=2000$ Hz. The

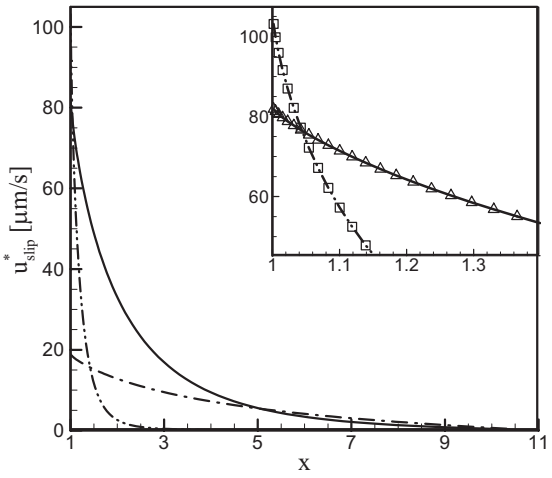

FIG. 3. Distribution of the dimensional slip velocity u_{slip}^* on the electrode surface obtained numerically by using the transformed-grid code for the electrolyte A at three frequencies, $f=2000$ Hz (dash-dot-dot lines and square symbols), 40 Hz (dash-dot), and 250 Hz (solid lines and delta symbols). The other parameters follow the standard set except for $x_m=y_m=11$ applied here. Symbols (squares for $f=2000$ Hz and deltas for $f=250$ Hz) are inserted in the zoom-in plot to indicate the clustering of grids near the electrode edge, $x=1$.

pattern is almost the same as the one that would be obtained without any potential drop across the Stern or inner layer; that is, the potential tends to be uniform over the electrode surface. Exceptionally, very near to the leading edge of the electrode, we expect a significant amount of disturbed potential contributed by alternating accumulation of ions and the subsequent charging in the inner layer, as is visualized distinctively at two instants, $t=2T/8$ and $6T/8$, in Fig. 4. Such localization of the charging and the slip velocity is more manifest at high frequencies. Figure 5 shows the time sequence of the ϕ field during one period obtained at a subcritical frequency, $f=100$ Hz. We can see that, compared with the supercritical case of Fig. 4, the surface potential with lower f reveals nonuniform distributions over the whole electrode surface. This then implies that spatial distribution of the slip velocity must be flatter at lower frequencies, as demonstrated in Fig. 3.

Figure 6 is prepared to illustrate the influence of the ac frequency f on the potential drop across the Stern layer $\Delta\phi_S$ and that across the inner layer $\Delta\phi_i$ and on the tangential gradient of the potential at the wall $\partial\phi_w/\partial s$ in order to understand the variation of the slip velocity u_{slip}^* upon change of f. As can be seen from Eq. (18), two important magnitudes that determine the instantaneous slip velocity u_s^* are $\Delta\phi_i$ and $\partial\phi_w/\partial s$. Since the final steady slip velocity u_{slip}^* is given from the time average of the instantaneous quantity, not only their magnitude but also their phase difference plays an important role in determining u_{slip}^*. For a supercritical f, the electrode potential changes its sign so frequently that ions do not have enough time to accumulate on the electrode surface. Thus $\Delta\phi_i$ remains at a low level as shown in Fig. 6(a). In the region far away from the leading edge the uniformity in the distribution of potentials is expected and therefore $\partial\phi_w/\partial s$ should also remain small; near the electrode edge, however,

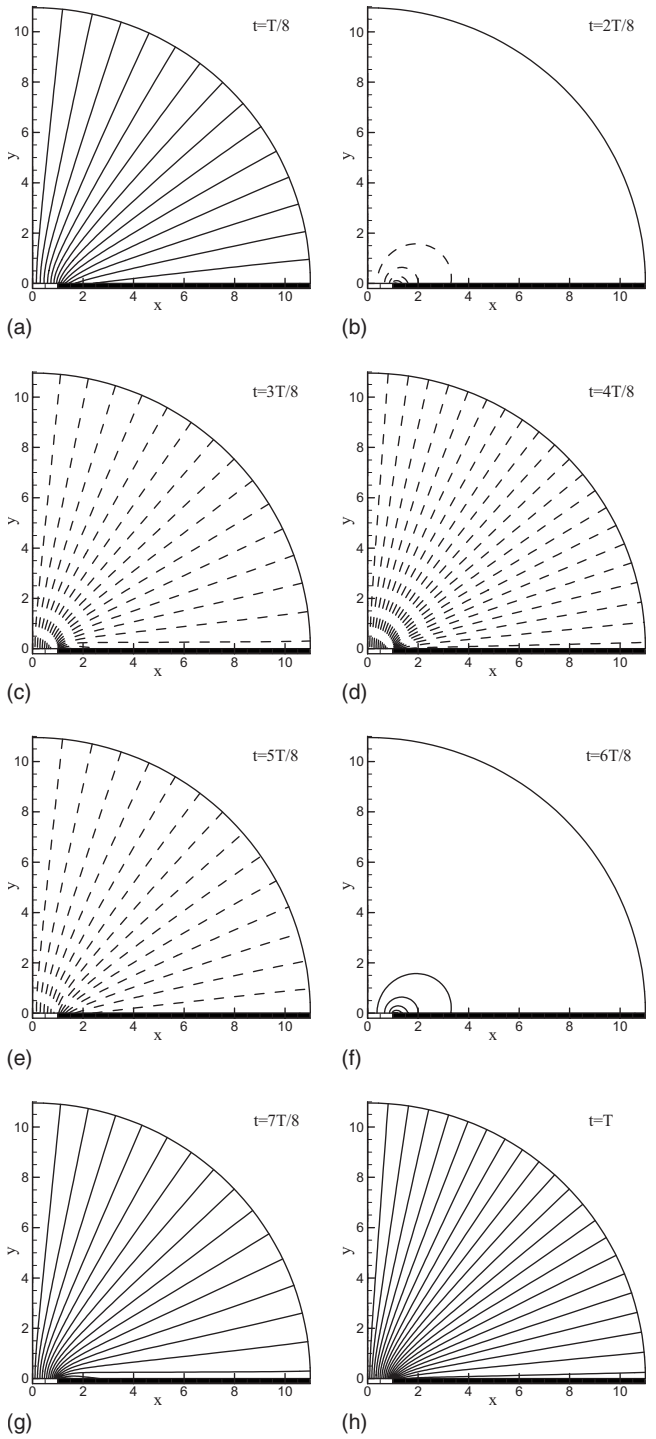

FIG. 4. Time evolution, during one ac period, of the spatial distribution of the potential field $\phi(x,y,t)$ obtained numerically at $f=2000$ Hz. All the other parameters are set at the same values as in Fig. 3. The increment of the potential in this contour plot is $\Delta\phi=0.0002$. The solid and the dashed lines denote the positive and negative contour levels, respectively; note that $\phi=0$ along the boundary $x=0$.

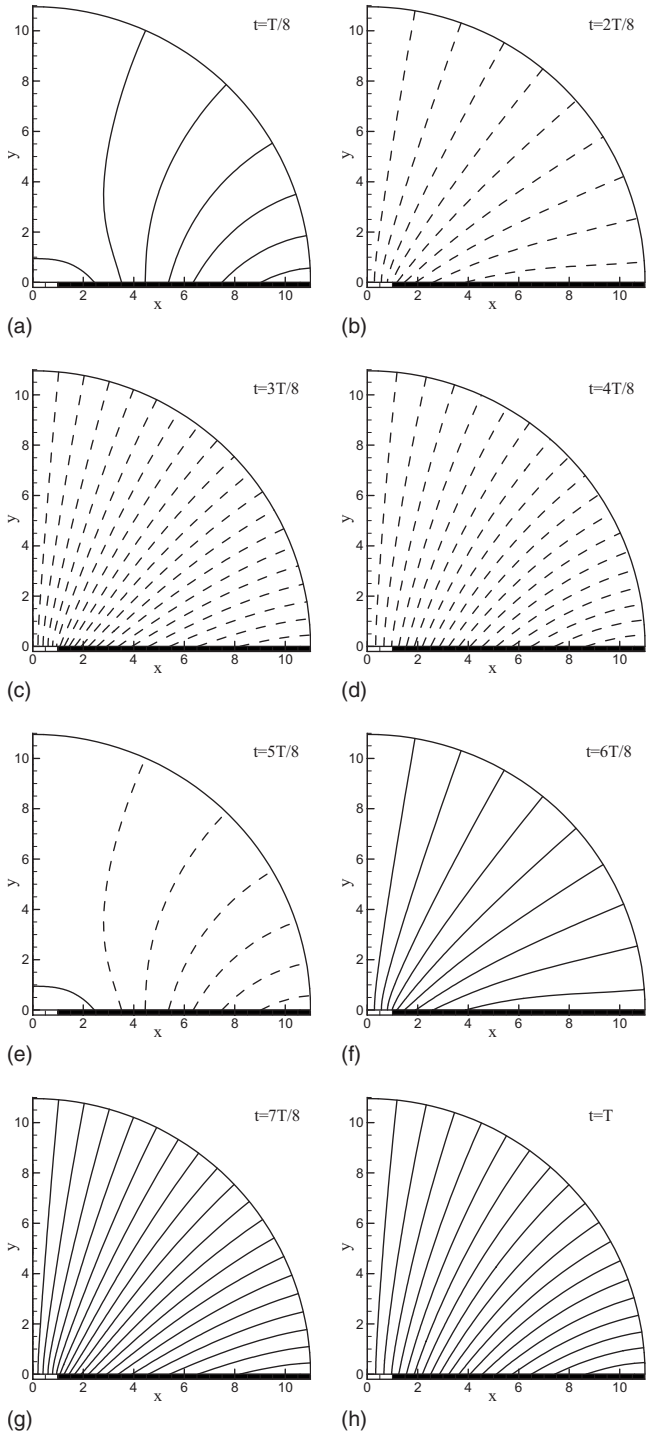

FIG. 5. Time evolution of $\phi(x,y,t)$ obtained numerically at $f=100$ Hz with all the other parameters set at the same values as in Fig. 3. The increment of the potential in this contour plot is $\Delta\phi=0.004$.

the potential drop occurs with a steep gradient which may give rise to a not-so-small value of $\partial\phi_w/\partial s$ as shown in Fig. 6(a). Conclusively, we can say that at high frequencies a low level of $\Delta\phi_i$ overall results in a small slip velocity, as was shown in Fig. 3. On the other hand, for a subcritical f, ions have enough time to accumulate on the electrode surface thereby showing the tendency to screen the electrode surface. Thus, we can find in this case a region near the leading edge of the electrode where the potential remains uniform with the magnitude close to zero, resulting in a small value of $\partial\phi_w/\partial s$ there as shown in Fig. 6(c). Further, the phase difference

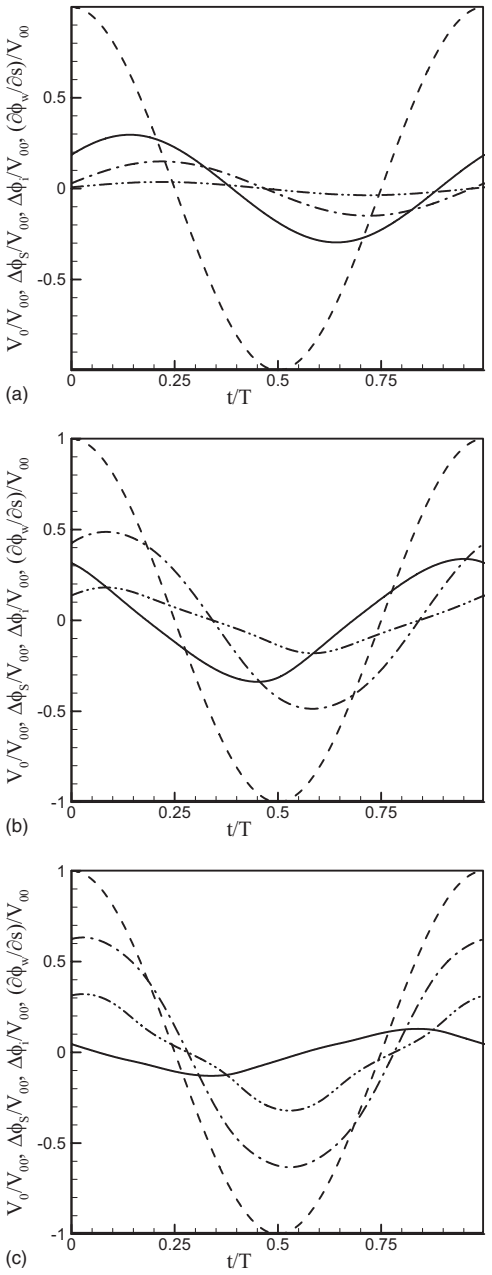

FIG. 6. Development of the external potential $V_0(t)$ (dashed lines), the potential drop across the Stern layer $\Delta\phi_S$ (dash-dot), that across the inner layer $\Delta\phi_i$ (dash-dot-dot), and the tangential gradient $\partial\phi_w/\partial s$ (solid) at a point, $x=1.421$, obtained numerically with the same parameter set as in Fig. 3 except for (a) $f=2000$ Hz (supercritical), (b) $f=250$ Hz (critical), and (c) $f=40$ Hz (subcritical) applied here; all four quantities are normalized by the amplitude of the external potential V_{00}.

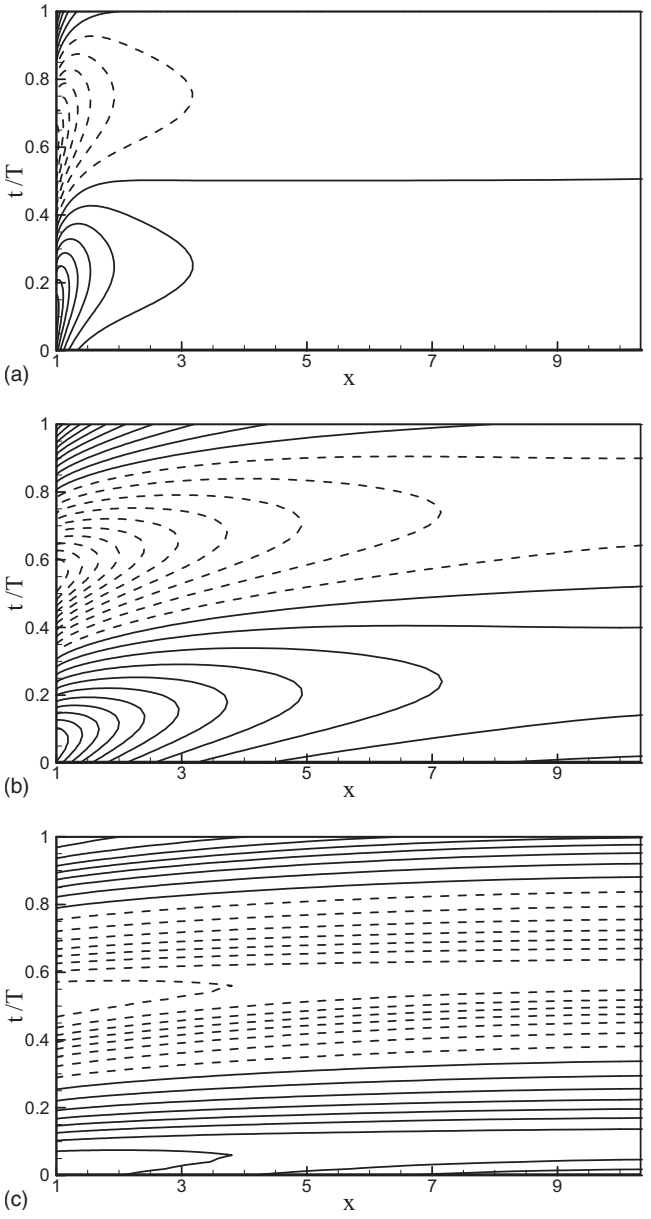

FIG. 7. Spatiotemporal distribution of $\Delta\phi_i/V_{00}$ at three frequencies; (a) $f=2000$ Hz with the contour increment 0.01; (b) $f=250$ Hz with the contour increment 0.02; (c) $f=40$ Hz with the contour increment 0.04. Here the contour lines with $\Delta\phi_i<0$ is shown as dashed lines. All the other parameters are set at same values as in Fig. 3.

between $\Delta\phi_i$ and $\partial\phi_w/\partial s$ is close to $T/4$, as also shown in Fig. 6(c). Conclusively with this case, $\Delta\phi_i$ is large but $\partial\phi_w/\partial s$ is small and the phase difference is close to $T/4$, which should again lead to a small slip velocity, as was shown in Fig. 3. Figure 6(b) corresponds to the case in between the two extreme situations, and it was shown in Fig. 3 that this critical case indeed gives the highest slip velocity.

Although Fig. 6 helps to comparatively understand the temporal change of $\Delta\phi_i$, $\Delta\phi_S$, and $\partial\phi_w/\partial s$ at one point, $x=1.421$, it cannot provide a global view of the spatiotemporal variation of them. Figure 7 demonstrates the dramatic difference in the spatiotemporal distribution of $\Delta\phi_i$ with f. It was found that the distribution of $\Delta\phi_S$ is very similar to $\Delta\phi_i$ except that the former is several times higher than the latter. At the supercritical state, Fig. 7(a), $\Delta\phi_i$ is maintained at a low level, and its variation is confined to the region close to the leading edge. Very close to the leading edge, it is shown that $\Delta\phi_i$ asymptotically has the same time phase as the external potential V_0; it seems that a very high electric field $\partial\phi/\partial n$ near the edge makes the charging occur in a very short time scale. Far from the edge, $\Delta\phi_i$ tends to lag the

external potential with the phase difference $T/4$; this is consistent with the linear response of the Debye layer under a small external potential, as shown by Suh and Kang [1]. This implies that at high frequencies, the region far from the leading edge reveals a linear behavior. On the other hand, at the subcritical state, Fig. 7(c), the level of $\Delta\phi_i$ is much higher than the supercritical case, but it tends to be uniform over the whole electrode surface; this implies that at the subcritical frequency a saturated charging has been reached. Therefore the gradient $\partial\phi_w/\partial s$ tends to be decreased in this regime as was shown in Fig. 6(c). On the other hand, at the critical frequency, Fig. 7(b), the level of $\Delta\phi_i$ not only remains at high values but also decreases smoothly as x is increased. The phase of $\Delta\phi_i$ also changes gradually from almost zero at the leading edge to approximately $T/4$ at the other end.

From the numerical results shown in Fig. 7, we can do some analysis to derive a simple formula that would predict the slip velocity qualitatively. First we note that $\Delta\phi_S$ and $\Delta\phi_i$ show similar patterns in both temporal and spatial distributions as can be seen from Fig. 6; we have also confirmed this from the comparison between Fig. 7 and the corresponding contour plots of $\Delta\phi_S$. So, we can write approximately as follows:

$$\Delta\phi_S = C\Delta\phi_i, \tag{22}$$

where the numerical constant C is typically $C=2-4$ depending on f for the above numerical results. Then from Eq. (8) the gradient $\partial\phi_w/\partial s$ can be obtained by using

$$\frac{\partial\phi_w}{\partial s} = -(1+C)\frac{\partial\Delta\phi_i}{\partial s}.$$

Substitute this into Eq. (18) to derive

$$u_s^* = -\frac{1+C}{2}\left(\frac{\varepsilon\varepsilon_0}{\mu L}\phi_{\mathrm{ref}}^{*2}\right)\frac{\partial(\Delta\phi_i)^2}{\partial s}. \tag{23}$$

Further, from observing the numerical results we assume the following form as the simplest approximation for the local spatiotemporal behavior of $\Delta\phi_i$:

$$\Delta\phi_i = B\exp(-ks)\cos(t-ms+\psi),$$

where the local coordinate s has its origin at an arbitrary point on the electrode surface and B denotes the amplitude of $\Delta\phi_i$ there. The constants k and m control the spatial rate of amplitude decay and phase change of $\Delta\phi_i$, respectively, and the constant ψ represents a local phase. Then we have

$$\left\langle -\frac{\partial(\Delta\phi_i)^2}{\partial s}\right\rangle = kB^2\exp(-2ks).$$

This indicates that the magnitude of the slip velocity is proportional to the spatial decay rate k and the square of the local amplitude of $\Delta\phi_i$, i.e., B. By using this simple fact, we can explain the fundamental cause of the results of Fig. 3 very easily from Fig. 7. For the supercritical case, Fig. 7(a), both k and B are at a low level over the whole electrode surface but increases sharply as the leading edge is approached. Therefore u_{slip}^* is large in this narrow region and remains small all over the other part of the electrode as shown by the corresponding line in Fig. 3. For the subcritical case, Fig. 7(c), B is large but k is small; in fact, as f is decreased there should be a limit in the increase of B (obviously the limit value is at most V_{00} occurring when the electrode is completely screened by the charging) but no limit in the decrease of k. Further, we observe from Fig. 7(c) that B is almost uniform over the whole range of x but k slowly decreases to reach zero at the end point $x=x_m$. This analysis should be enough to understand the slow decrease of the slip velocity being maintained at a low level for the supercritical frequency in Fig. 3. Finally, for the case of the critical frequency, Fig. 7(b), B is smaller but k is significantly larger than the supercritical regime, which eventually leads to the highest slip velocity in a wide region as shown in Fig. 3.

C. Effect of the electrode length and the domain size

In this subsection, we address the effect of the size of the electrode and the domain on the numerical results. First, we studied on the effect of the electrode length on the slip velocity. While keeping the domain size at $x_m=32$, we changed the electrode length by adjusting the coordinate of the electrode's trailing edge x_{em}. Shown in Fig. 8(a) is distributions of u_{slip}^* along the electrode surface obtained for two electrodes, $x_{em}=5$ and 10, and two frequencies, $f=100$ and 1000 Hz. At the low frequency, $f=100$ Hz, the fluid slip occurs in a broad range of the electrode surface, whereas at the high frequency, $f=1000$ Hz, it tends to be confined to the region close to the leading edge, which is in line with the discussions given in the previous subsection. Because of this, the electrode size exerts almost no effect at high frequencies but significant effect at low frequencies on the slip velocity. In the latter case, a shorter electrode produces a lower level of u_{slip}^*. Figure 8(b) shows the slip velocities u_5^* and u_{10}^* obtained by fixing the domain size at $x_m=32$ while changing the electrode length from $x_{em}=3$ to 32 at two frequencies. It again indicates that the effect of the electrode size is more pronounced at lower frequencies. The reason for a lower level of u_{slip}^* with a shorter electrode at subcritical frequencies can be understood from the spatiotemporal distributions of $\Delta\phi_i/V_{00}$ shown in Fig. 9. This figure indicates that the magnitude of $\Delta\phi_i/V_{00}$ obtained with a shorter electrode, $x_{em}=5$ [Fig. 9(a)], is somewhat larger than that with the longer electrode [Fig. 9(b)], but its spatial variation for the shorter one is weaker than that for the longer one. This means that a longer electrode provides a smaller B but a larger k, which resultantly gives a larger slip velocity as shown in Fig. 8. The fact that the magnitude of $\Delta\phi_i$ remains almost uniform over the whole electrode surface for a shorter electrode can be further understood from the distribution of $-(\partial\phi/\partial n)_w$, the normal component of the electric field at the electrode surface, which is presented in Fig. 10. This figure shows that $-(\partial\phi/\partial n)_w$ is higher for shorter electrodes. On the other hand, we can observe that the spatial gradient of $-(\partial\phi/\partial n)_w$ along the coordinate x is lower for shorter electrodes. It is clear from the physical intuition or from Eqs. (9b) and (11) that the potential drop $\Delta\phi_i$ is proportional to the magnitude of $-(\partial\phi/\partial n)_w$. So, we can expect a higher level but smaller spatial gradient of $\Delta\phi_i$ for shorter electrodes. In this case, the consequence of the decrease of the

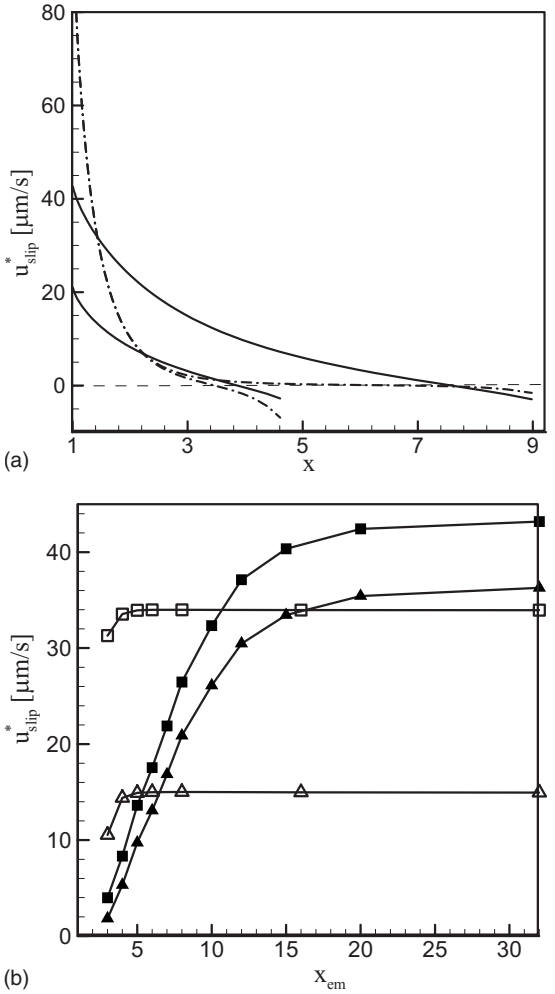

FIG. 8. Effect of the electrode size on the slip velocity u^*_{slip} with the domain size fixed at $x_m=32$; (a) distributions of u^*_{slip} along the electrode with $x_{em}=5$ (upper lines) and 10 (lower lines) at $f=100$ (solid lines) and 1000 Hz (dash-dot lines); (b) magnitude of u^*_5 (squares) and u^*_{10} (deltas) as functions of x_{em} at $f=100$ Hz (filled) and $f=1000$ Hz (empty). All the other parameters are set at the same values as in Fig. 3.

spatial gradient seems to dominate over that of the increase of the magnitude itself, which is the fundamental reason for the decrease of the slip velocity for shorter electrodes.

Next we studied on the effect of the domain size. While keeping the electrode's end position at $x_{em}=9$, we changed the domain size from $x_m=9$ to 32. The variation of the slip velocities u^*_5 and u^*_{10} is plotted in Fig. 11. At the high frequency $f=1000$ Hz, the slip velocities do not show any significant variation. At the low frequency $f=200$ Hz, however, they are increased for smaller domain size. This also indicates that the domain size affects the slip velocity only at low frequencies.

D. Effect of the Stern-layer thickness

In this subsection we study the effect of the effective thickness of the Stern layer λ_{Seff} on the slip velocity. In this simulation, we set $x_m=x_{em}=41$ following the experimental

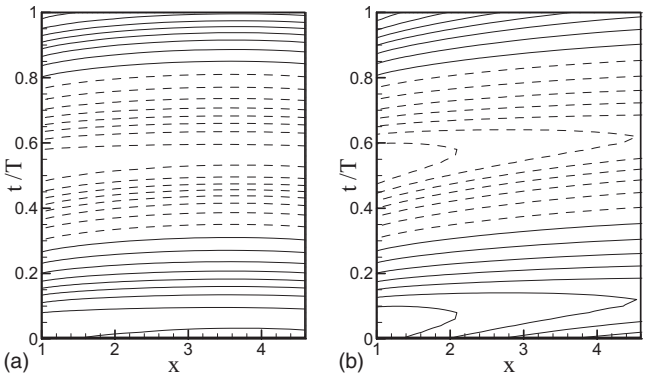

FIG. 9. Comparison of the spatiotemporal distributions of $\Delta\phi_i/V_{00}$ obtained at $f=100$ Hz for two electrode lengths; (a) $x_{em}=5$; (b) $x_{em}=10$. The domain size is fixed at $x_m=32$. The contour increment for both plots is 0.04. In (b), the range of x for the plot was set as the same as (a) for direct comparison between the two.

setup of Green *et al.* [13]. Figure 12 illustrates the numerical results given with no adsorption effect for various values of λ_{Seff}. It shows that as λ_{Seff} increases the slip velocity u^*_5 is decreased substantially in the subcritical regime while it is slightly increased in the supercritical regime, which overall leads to the increase of f_c. The numerical result with $\lambda_{Seff}=60$ nm produces the peak value of u^*_5 in almost the same level as that measured by Green *et al.* [13], but the numerical f_c is almost ten times larger than the experimental one. Therefore we can see that for any choice of λ_{Seff} the experimental data cannot be reproduced with a suitable level of accuracy for the case without the adsorption effect.

The reason for the decrease of the slip velocity with λ_{Seff} in the subcritical regime can be explained with the aid of the spatiotemporal distributions of $\Delta\phi_i$ and $\Delta\phi_S$, as shown in Fig. 13. First note that, if we were to use Eq. (23) in this analysis, the parameter C is no longer constant; it is zero for $\lambda_{Seff}=0$ but close to 1 for $\lambda_{Seff}=10$ nm. Therefore we had

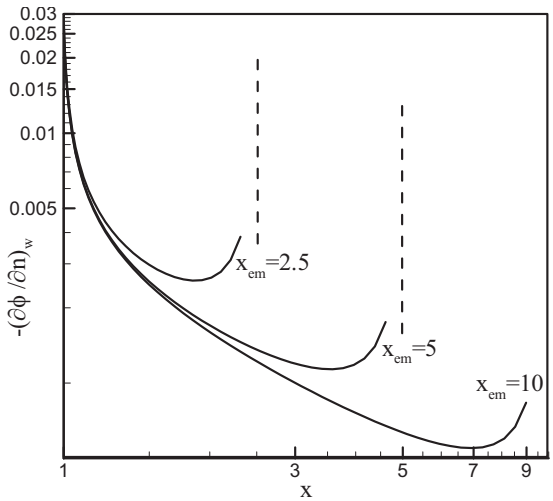

FIG. 10. Distributions of $-(\partial\phi/\partial n)_w$, the normal component of the electric field at the electrode surface, obtained with $f=100$ Hz for three electrode lengths at the very beginning of the simulation $t=0$ when no charging occurs. All the other parameters are set at the same values as in Fig. 3.

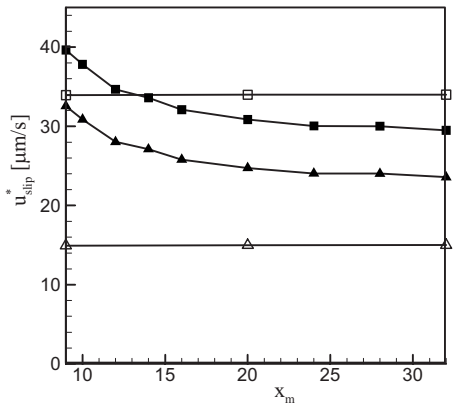

FIG. 11. Effect of the domain size x_m on the slip velocity u_5^* (squares) and u_{10}^* (deltas) obtained at $f=100$ Hz (filled) and $f=1000$ Hz (empty). Here the electrode length is fixed at $x_{em}=9$. All the other parameters are set at the same values as in Fig. 3.

better use the original form (18) rather than Eq. (23) in studying the effect of the Stern layer. By comparing Figs. 13(a) and 13(b) we can detect the decrease of $\Delta\phi_i$ due to the Stern-layer effect. On the other hand, the magnitude of $\Delta\phi_S$ is comparable to that of $\Delta\phi_i$ as shown in Fig. 13(c). Although each of the two potential drops for $\lambda_{Seff}=10$ nm may be smaller than $\Delta\phi_i$ for $\lambda_{Seff}=0$, the total potential drop is found to be larger for $\lambda_{Seff}=10$ nm. This then implies [see Eq. (8)] that ϕ_w should be decreased due to the Stern-layer effect. From these and other results we can state that, for subcritical frequencies, the presence of the Stern layer causes a decrease of both $\Delta\phi_i$ and ϕ_w causing the slip velocity to decrease, following Eq. (18).

Sketches of Fig. 14 are prepared to compare the dramatic difference in the potential distribution for three cases. Consider a point on the electrode wall and an instant when the external potential is $V_0(t)$ and the potential at the outer edge of the inner layer is ϕ_w. A typical distribution of the potential

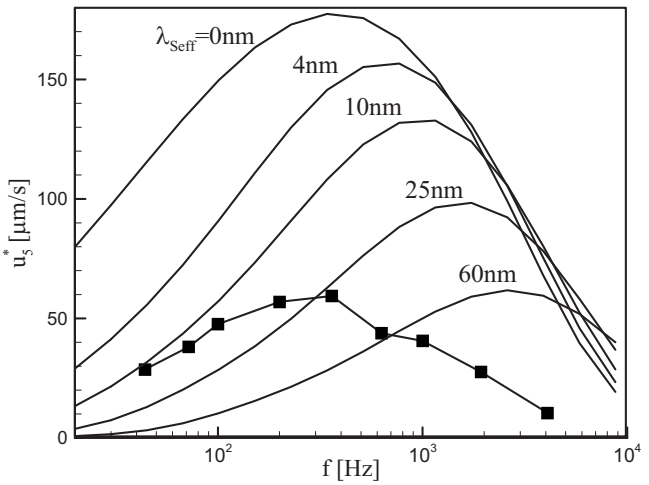

FIG. 12. Influence of λ_{Seff}, the effective Stern-layer thickness, on the slip velocity u_5^* in the frequency domain. Here no adsorption effect was assumed, i.e., we set $\Gamma^*_{max}=\alpha^*=0$. The domain size and the electrode length are set at $x_m=x_{em}=41$. The experimental data given by Green *et al.* [13] are denoted by symbols.

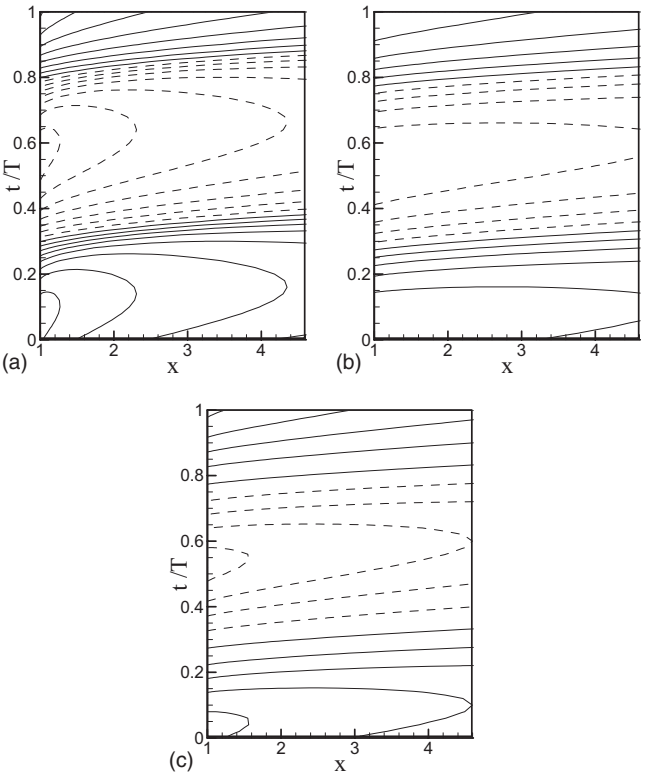

FIG. 13. Spatiotemporal distributions of normalized potential drops obtained without adsorption effect at $f=100$ Hz; (a) $\Delta\phi_i/V_{00}$ for $\lambda_{Seff}=0$ (without Stern layer), (b) $\Delta\phi_i/V_{00}$ for $\lambda_{Seff}=10$ nm, and (c) $\Delta\phi_S/V_{00}$ for $\lambda_{Seff}=10$ nm. The contour increment is 0.1.

within the inner layer for the case without the Stern layer may look like Fig. 14(a) and the potential drop across the inner layer should read $\Delta\phi_i=V_0-\phi_w$. Then we insert a Stern layer at the interface between the electrode and the inner layer, like Fig. 14(b), within which the potential shows a linear distribution (no charging); here the thickness of the inserted Stern layer is supposed to be the effective thickness, not the actual thickness, the dimensional quantity being λ_{Seff} [refer to Eq. (10) for the relation between the two thicknesses]. We also assume momentarily that ϕ_w is the same as in Fig. 14(a) and the amount of charging is unchanged too. Then $\Delta\phi_i$ must be reduced because now $\Delta\phi_i=V_0-\phi_w-\Delta\phi_S$. Of course ϕ_w itself should be modified when the Stern-layer effect is considered, but its effect can be assumed to be secondary. Figure 14(c) will be discussed in the next section when the effect of the adsorption is addressed.

E. Effect of the adsorption and comparison with experimental data

It was shown numerically in the previous section that any choice of the Stern-layer thickness cannot reproduce the experimental data. In this section we will see that a suitable choice of the adsorption parameters can give rise to fairly good agreement between the two results. Presented in Fig. 15 is the slip velocity u_5^* obtained numerically for the various values of Γ^*_{max} at $\alpha^*=3.16\times10^{-23}$ m^3 in Fig. 15(a) and for the various values of α^* at $\Gamma^*_{max}=5\times10^{16}$ m^{-2} in Fig. 15(b).

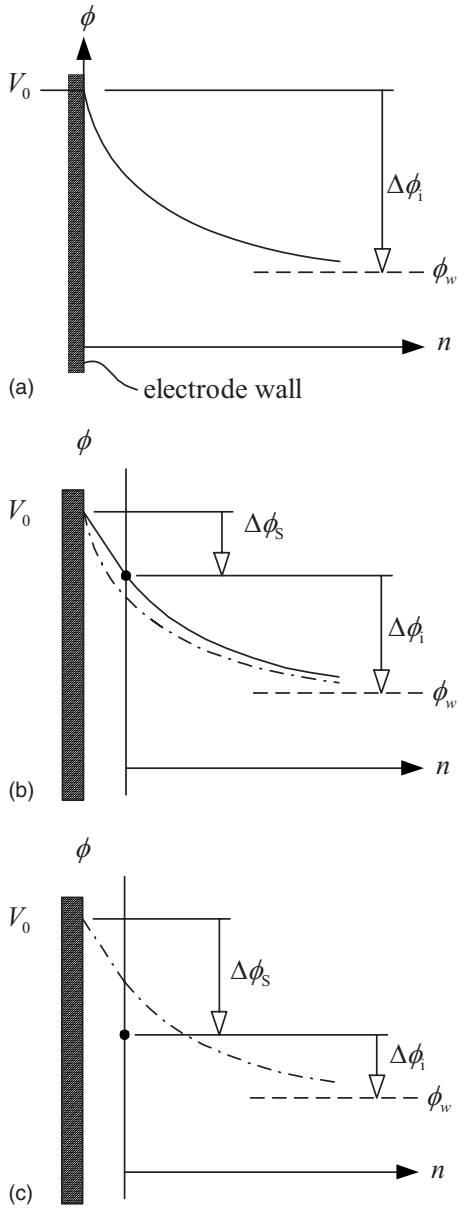

FIG. 14. Sketches illustrating the potential distribution (solid lines) and its drop near the electrode (hatched) surface (a) without the Stern-layer or adsorption model, (b) only with the Stern-layer model, and (c) with both the Stern-layer and adsorption models. In these plots the horizontal dashed line denotes the asymptotic value of the potential at the outer edge of the inner layer, i.e., ϕ_w. The dash-dot line in (b) corresponds to the solid line of (a) and the dash-dot line of (c) to the solid line of (b).

We see from Fig. 15(a) that an increase of Γ^*_{max} results in a decrease of the slip velocity, as expected. With $\Gamma^*_{max}=5\times10^{16}$ m^{-2}, the numerical results show good agreement with the experimental results. An increase of Γ^*_{max} also causes a decrease of the critical frequency. The effect of α^* on the slip velocity with fixed Γ^*_{max} is similar to that of Γ^*_{max} with fixed α^*, as can be seen from Fig. 15(b). In this case, however, the slip velocity is saturated at α^* larger than the value $\alpha^*=3.16\times10^{-23}$ m^{-3}. Further discussion on such saturation of the slip velocity will be given later in this section.

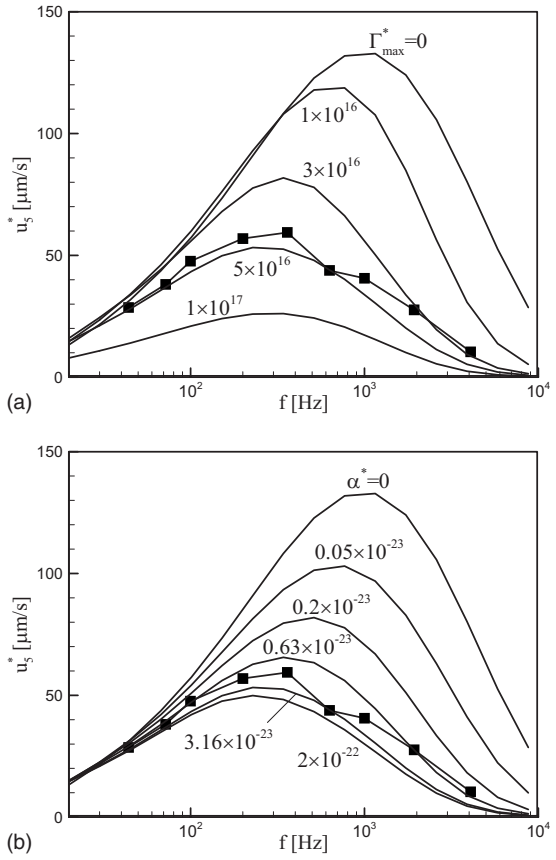

FIG. 15. Effect of the adsorption parameters on the slip velocity u^*_s: (a) effect of Γ^*_{max} at $\alpha^*=3.16\times10^{-23}$ m^3; (b) effect of α^* at $\Gamma^*_{max}=5\times10^{16}$ m^{-2}. The experimental data given by Green *et al.* [13] are denoted by symbols.

The reason for the decrease of the slip velocity with introduction of the ion adsorption can be explained as follows. First we note that (counter)ions are adsorbed at the interface between the Stern and inner layers causing an increase of the surface charge there. Integration of the Poisson equation (4) across the very thin layer on the interface, where ions are adsorbed, then tells us that there is a jump in the potential gradient on both sides of the interface as shown in Fig. 14(c); this jump is proportional to the amount of adsorption. Therefore the potential drop across the inner layer must be decreased, which finally makes the slip velocity decreased.

Figure 16 shows the slip velocities obtained by the numerical simulation for the electrolytes A and B with the adsorption parameter values chosen to give the best fit with the experimental data of Green *et al.* [13]. Both the slip-velocity magnitude and the critical frequency of the measurement are well reproduced by the numerical simulation. It is also remarkable to note that both fittings have been established with the same values of Γ^*_{max} and α^*.

The optimum parameter set used for the data of Fig. 16 was in fact obtained from the parametric study on the rms error ε^*_{rms} of the slip velocity. Here the ε^*_{rms} is defined as the root-mean-square of the numerical slip velocities referring to the experimental data u^*_m $(m=5,10,15,20)$ of Green *et al.* [13]. In order to find the parameter set for the best agreement between the numerical and experimental slip velocities, we

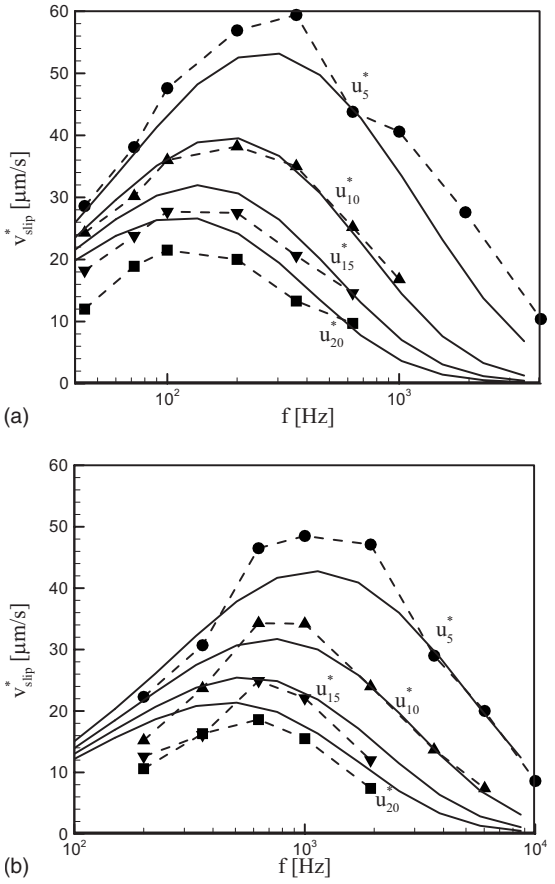

FIG. 16. Comparison of the slip velocities u^*_{slip} obtained by the present numerical method at the standard parameter set (solid lines) with those of the experimental measurement reported by Green *et al.* [13] (symbols linked by dashed lines) for (a) electrolyte A and (b) B.

first set the parameter α^* at a certain value. While changing the parameter Γ^*_{max}, we find the critical value of Γ^*_{max} at which ε^*_{rms} becomes minimum. We repeat this process for the other values of α^*. Figure 17 shows the locus of $(\Gamma^*_{max}, \alpha^*)$ obtained in this way for the electrolytes A and B at three different values of λ_{Seff}. We recognize two distinctive regimes from this plot. The first one corresponds to the parameter space $\alpha^* > 10^{-23}$ m^3 approximately in which the locus is almost vertical. In this regime the best parameter set is determined solely by Γ^*_{max} and variation of α^* exerts almost no influence on the error. This can be understood from the formula for the parameter β representing the adsorption effect, i.e., Eq. (12). In the first regime, α is large enough that Eq. (12) can be approximated like $\beta \cong 8\Gamma_{max}/q$ under the assumption $\langle \gamma q^2 \rangle \gg \alpha \gg 1$. In the second regime, $\alpha^* < 10^{-23}$ m^3, the locus can be simply written as $\alpha^* \Gamma^*_{max} \cong$ const. This can also be understood from the approximation of Eq. (12) under the assumption $\alpha \ll 1$ and $\langle \gamma q^2 \rangle \ll 1$. The figure also reveals that as the Stern-layer thickness increases, the value Γ^*_{max} must be decreased with the value of α^* being fixed for the best fit to the experimental data. On the other hand, higher concentrations turn out to require lower Γ^*_{max} and/or lower α^*.

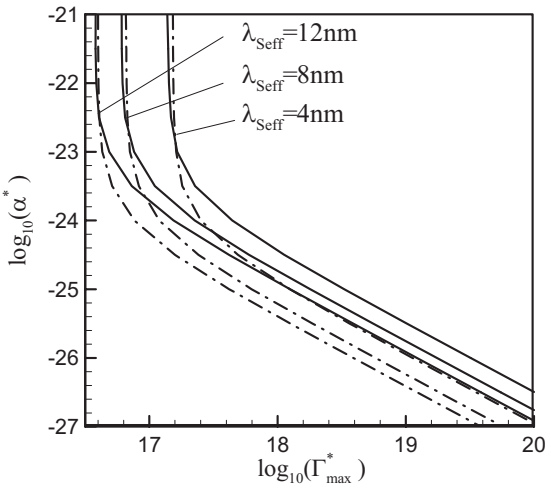

FIG. 17. Locus of the parameter set $(\Gamma^*_{max}, \alpha^*)$ at which the rms error of the slip velocity becomes locally minimum when Γ^*_{max} is varied while α^* is fixed with three values of λ_{Seff}. The solid and dash-dot lines are for electrolytes A and B, respectively.

So far we have seen that the adsorption phenomenon can give rise to good agreement in the slip velocity between the numerical calculation and the experimental measurement. Considering that all the previous numerical simulations or theoretical analyses overpredict the measured results by one or two order of magnitude, good agreement between those data as shown in Fig. 16 is very encouraging. Regarding the still-existing discrepancy between the two results, we need to address one point of view. Green *et al.* [13] mentioned that while doing experimental measurement of the ac electroosmotic flows, particles were sticking on the electrode surfaces. Obviously, the effective size of the electrodes should have been decreased in that case. Unfortunately, no information has been reported as to the extent and range of the covered portion of the electrodes. Further, the fact that shorter electrodes cause the slip velocity lower at subcritical frequencies, as addressed in the previous subsection, does not seem to enhance the matching between the two data.

F. Further discussions

The numerical results presented so far have been obtained at the parameter sets corresponding to weakly nonlinear regimes. In this subsection we will investigate the numerical results of a strongly nonlinear case and understand how the weakly nonlinear model breaks down for such cases. Figure 18(a) exhibits the temporal change of the wall potential ϕ_w obtained from the interactive 2D calculation in comparison with that obtained from the 1D PNP (Poisson-Nernst-Planck) numerics for a weakly nonlinear case without an adsorption effect. Here, the 1D PNP calculation employs the 1D version of the Nernst-Planck equations (3) for the concentration dynamics and the 1D version of the Poisson equation (4) for the potential; a detailed description of the numerical method has been given in [1]. The time history of the potential gradient at the electrode wall, $(\partial\phi/\partial y)_w$, obtained from the interactive 2D calculation (dashed line in the figure) serves as one of the boundary conditions at the outer edge of the domain in the

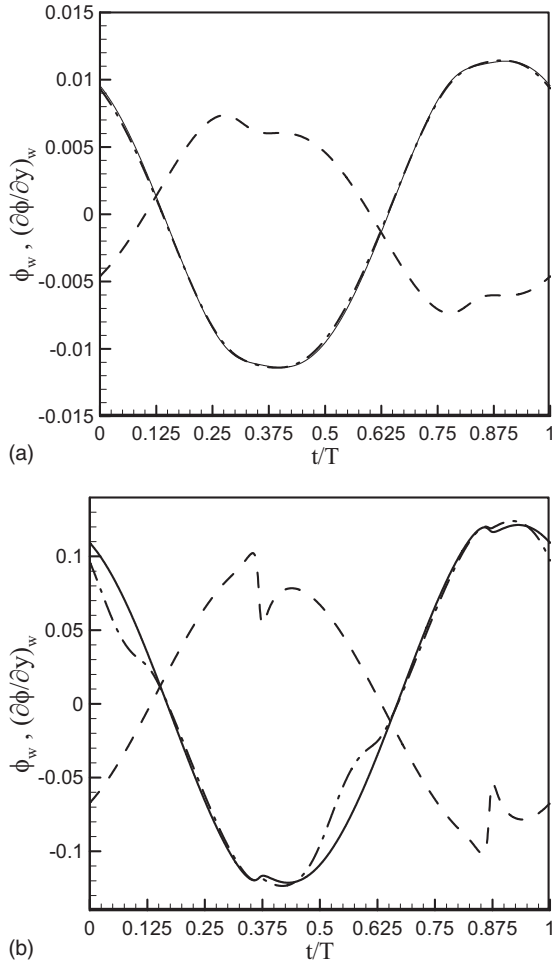

FIG. 18. Comparison between $\phi_w(t)$ obtained at $x=1.414$ from the interactive 2D calculation (solid) and that obtained from the full 1D calculation (dash-dot) with the potential gradient at the edge of the domain being provided by the 2D calculation (dashed) for (a) a weakly nonlinear case with $V_{00}^*=0.25$ V and (b) a strongly nonlinear case with $V_{00}^*=2$ V. The other parameter values are the same as the standard set except for the following: $f=500$ Hz and $\Gamma_{\max}^*=\alpha^*=0$ (no adsorption).

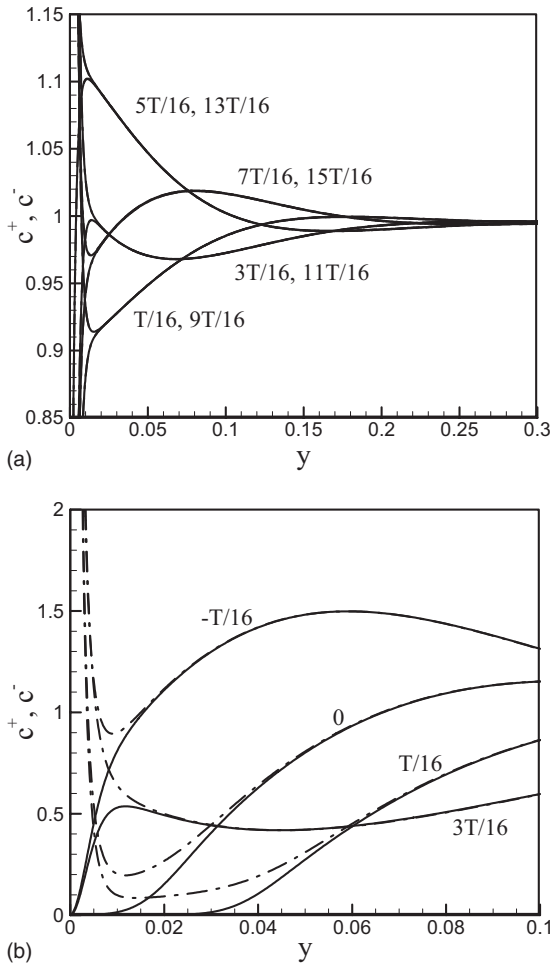

FIG. 19. Development of the cation (solid) and anion (dash-dot) concentrations within the middle layer obtained from the full 1D calculation with the condition given in the caption of Fig. 18; (a) a weakly nonlinear case with $V_{00}^*=0.25$ V and (b) a strongly nonlinear case with $V_{00}^*=2$ V.

1D calculation and the asymptotic potential ϕ_w (see Fig. 14), to be compared with that obtained from the interactive 2D calculation, is given by extrapolating the linear distribution of the potential in the bulk and middle layer and evaluating at the wall $y=0$. It clearly reveals exact agreement between the two results for the weakly nonlinear case. The nonlinearity of the physics becomes more prevalent at the point closer to the leading edge and at lower frequencies. The external potential is also another factor that affects the nonlinearity. Figure 18(b) demonstrates the numerical results given at a higher external potential. The distribution of ϕ_w obtained by the 2D calculation now deviates from the 1D PNP result in particular for $0 \leqslant t/T \leqslant 1/8$ and $1/2 \leqslant t/T \leqslant 5/8$. The reason is due to the non-neutral character of the middle layer as explained below.

Figures 19(a) and 19(b) show the development in time of the spatial distributions of the concentrations in the middle layer for weakly and strongly nonlinear cases, respectively. Since the diffusivity and frequencies are the same for both cases, the middle layer extends from the electrode wall with the same distance, say up to $y \cong 0.3$ or $y^* \cong 3.8$ μm; on the other hand, the inner layer is measured to span only up to $y \cong 0.02$ or $y^* \cong 0.25$ μm. For the weakly nonlinear case [Fig. 19(a)], both the cation and anion concentrations deviate only slightly from the bulk value 1 in the middle layer. More importantly, the two ions show temporally identical distributions leading to the neutralized character of the layer. Therefore this result does not contradict the assumptions required for the asymptotic analysis for the weakly nonlinear cases which is employed in our 2D calculation, and so the agreement between the two results was excellent, as shown in Fig. 18(a). It also implies that the small nonzero concentration gradient shown in Fig. 19(a) should provide a negligible effect on the validity of the Laplace equation (7) for the middle layer. On the other hand, the strongly nonlinear case [Fig. 19(b)] reveals significantly different distributions between the two ions. During the interval $0 \leqslant t/T \leqslant 1/8$, the anion shows a higher concentration than the cation in the middle layer; the results of $t/T=1/8$ are similar to those of $t/T=1/16$ but are not shown in the figure to avoid confusion. As

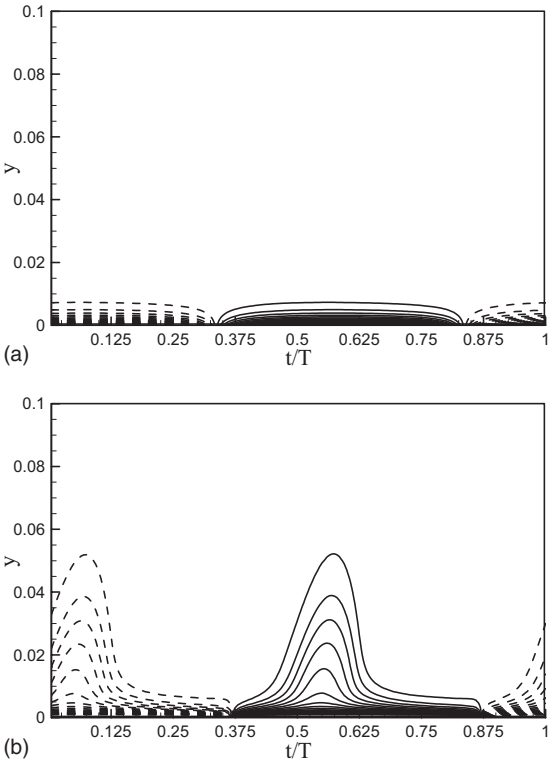

FIG. 20. Spatiotemporal distribution, within the inner and middle layers, of the perturbed potential gradient $\partial\phi/\partial y - (\partial\phi/\partial y)_w$ obtained from the 1D PNP calculation with the condition given in the caption of Fig. 18; (a) a weakly nonlinear case with $V_{00}^*=0.25$ V and (b) a strongly nonlinear case with $V_{00}^*=2$ V. The contour levels are 0.1, 0.3,… for positive values (solid) and −0.1,−0.3,… for negative values (dashed).

explained in [1], during this interval, the anions are attracted to the electrode while the cations are repelled from it. Simultaneously, the bulk gives anions to and takes cations from the middle layer through the conduction process. Since the electrode does not need the cations, complete depletion of the cations can take place starting from the inner-layer side during this interval; Fig. 19(b) shows that the depletion extends to $y \cong 0.03$ at $t/T=1/16$. On the other hand, the anions are still required by the inner layer during this interval, and so the anion concentration must show a nonzero level in order for the conduction process to take place conveying the cations from the bulk to the inner layer; since the distribution of the cation concentration is almost flat near the inner-layer side, transport of ions by the diffusion is almost negligible there.

Non-neutralized distribution of the middle layer makes the layer charged contrary to the basic assumptions made for the asymptotic analysis, and this in turn results in the nonuniform potential gradient in the middle layer. Figures 20(a) and 20(b) show spatiotemporal distributions of the perturbed potential gradient, $\partial\phi/\partial y - (\partial\phi/\partial y)_w$, obtained from the 1D PNP calculation. For the weakly nonlinear case, Fig. 20(a), its magnitude remains almost zero all over the middle layer indicating the neutralized middle layer. For the strongly nonlinear case, Fig. 20(b), however, the potential gradient differs from that of the bulk over a significantly wide range of space especially for the time intervals, $0 \leqslant t/T \leqslant 1/8$ and $1/2 \leqslant t/T \leqslant 5/8$. During the interval $0 \leqslant t/T \leqslant 1/8$, the potential gradient in the bulk $(\partial\phi/\partial y)_w$ itself is negative, and so $\partial\phi/\partial y$ is also negative and its magnitude should be larger than that of $(\partial\phi/\partial y)_w$. Considering the fact that the potential gradients in the Stern and inner layers are almost unaffected by the middle-layer charging and the potential during the given time interval remains positive everywhere, we can understand that the magnitude of the potential at the outer edge of the middle layer $|\phi_w|$ must be decreased by the middle-layer charging during the given time interval, as shown in Fig. 18(b). The situation is reversed for the other time interval $1/2 \leqslant t/T \leqslant 5/8$, and we can also understand the decrease of $|\phi_w|$, as shown in Fig. 18(b).

The concentration polarization found in the transport of ions through ion-exchange membranes [21–26] or nanochannels [27,28] is also known to reveal similar phenomenon. In general, at a steady state one side of the perm-selective membrane shows enrichment of ions whereas the other side shows depletion of ions; but both sides are still neutralized at low external potentials. However, when the external potential is increased the depletion side shows complete depletion of anions (for the case where the cations are selected to pass through the membrane), and the cation distribution there becomes almost uniform at a low level; this region is called the "extended space charge" region [23]. In the present study we measure from Fig. 20(b) that this region extends to as much as $y \cong 0.05$ or $y^* \cong 63$ nm, if we select 0.1 as the magnitude of the contour level for the border between the extended-space-charge region and the remaining neutralized middle layer. Interestingly enough that region is reported to produce electro-osmotic flow of the second kind [23], which allows the overlimiting current and the enhancement of mixing [27] through the electroconvective instability [23]. It will be interesting to work on this possibility for the ac electroosmotic flows, too.

IV. CONCLUSIONS

In this paper we have presented the numerical method for obtaining the slip velocity distribution on the electrode walls for ac electro-osmotic flows. The algorithm interactively solves the Laplace equation for the bulk potential and the dynamical equation for the surface charge density on the electrode wall. We have developed both explicit (for the Cartesian coordinates) and implicit (for the curvilinear coordinates) methods in coupling the two equations. In the former method, the surface charge density is first obtained by solving the dynamical equation, which is then used to calculate the potential drops across the Stern and inner layers and the accumulation of charges at the interface between the two layers. Those results are then used in determining the potential at the electrode walls, which is next used as boundary conditions for the Laplace equation. The solution of the Laplace equation then provides normal gradient of the potential on the electrode walls, which is in turn used in solving the dynamical equation for the surface charge density. In the implicit method, the dynamical equation is solved simultaneously in coupling with the Laplace equation. Such an im-

plicit treatise of the variables avoids the numerical instability encountered in the explicit method when the grid size is decreased to resolve the region near the leading edge of the electrodes.

The code is then applied to a 2D problem around coplanar electrodes under ac. We first validated our code by observing a slight variation of numerical results upon grid refinement. Further validation is confirmed by comparing the numerical results given from the Cartesian coordinates and those from the transformed coordinates.

The effect of the ac frequency on the slip velocity was shown to be distinctively different for the subcritical and supercritical cases. At subcritical frequencies, slow variation of the electrode potential allows relatively long time for the ions to charge and screen the electrode interfaces so that the slip velocity remains at low level with flat distribution. On the contrary, at supercritical frequencies, fast switching of the electrode potential does not allow enough time for the ions to charge the inner layer except for the region near the leading edge, where intense normal gradient of the potential compensates the short-time charging. Therefore the supercritical frequency yields sharp variation of the slip velocity near the leading edge. The fundamental reason for such difference in the slip velocity distribution is further addressed by using the spatiotemporal distribution of the potential drops and simplified equations.

The electrode length has almost no effect on the slip velocity at supercritical frequencies, but a significant effect is expected at subcritical frequencies giving smaller slip velocity with shorter electrodes.

An increase of the Stern-layer thickness is found to bring the decrease of the slip velocity and increase of the critical frequency. However, simply adjusting the Stern-layer thickness cannot successfully match the numerical results with the experimental ones.

Since the ion adsorption causes a jump in the normal gradient of the potential at the interface between the Stern and inner layers, the amount of the potential drop in the inner layer can be decreased without bound by increasing either one or both of the two adsorption parameters. This in turn leads to a decrease of the slip velocity. It was found that while the slip velocity is decreased without bound with an increase of the parameter $\Gamma^*_{\max}$, the decrease of the slip velocity is saturated with the increase of the parameter α^* above a critical vale.

Although our adsorption model turned out to result in a very successful match between the numerical and experimental data for the slip velocity, the relevance of the adsorption phenomenon must be proved in the physicochemical point of view probably through the use of the experimental measurement and/or observation. We also need experimental studies and/or molecular-dynamic simulations to collect data for the effect of the various parameters such as the surface roughness of electrodes on the adsorption phenomenon.

Our 2D calculation results are in excellent agreement with those of the 1D PNP calculation at a weakly nonlinear regime. For a strongly nonlinear case, however, the two results show a discrepancy at particular intervals of time, at which in the middle layer co-ions are completely depleted and the counterions are almost uniformly distributed at a low level, the phenomenon being similar to the so called extended-space-charge region coined by the researchers involved in the perm-selective membranes.

ACKNOWLEDGMENTS

This work was supported by the Korea Science and Engineering Foundation (KOSEF) through the National Research Laboratory Program funded by the Ministry of Science and Technology (Grant No. 2005-1091).

[1] Y. K. Suh and S. Kang, Phys. Rev. E **77**, 031504 (2008).
[2] A. Ajdari, Phys. Rev. E **61**, R45 (2000).
[3] A. B. D. Brown, C. G. Smith, and A. R. Rennie, Phys. Rev. E **63**, 016305 (2000).
[4] V. Studer, A. Pepin, Y. Chen, and A. Ajdari, Microelectron. Eng. **61-62**, 915 (2002).
[5] V. Studer, A. Pepin, Y. Chen, and A. Ajdari, Analyst (Cambridge, U.K.) **129**, 944 (2004).
[6] M. Mpholo, C. G. Smith, and A. B. D. Brown, Sens. Actuators B **92**, 262 (2003).
[7] L. H. Olesen, H. Bruus, and A. Ajdari, Phys. Rev. E **73**, 056313 (2006).
[8] A. Brask, D. Snakenborg, J. P. Kutter, and H. Bruus, Lab Chip **6**, 280 (2006).
[9] M. Bazant and Y. Ben, Lab Chip **6**, 1455 (2006).
[10] J. P. Urbanski, T. Thorsen, J. A. Levitan, and M. Z. Bazant, Appl. Phys. Lett. **89**, 143508 (2006).
[11] J. P. Urbanski, J. A. Levitan, D. N. Burch, T. Thorsen, and M. Z. Bazant, J. Colloid Interface Sci. **309**, 332 (2007).
[12] A. Gonzalez, A. Ramos, N. G. Green, A. Castellanos, and H. Morgan, Phys. Rev. E **61**, 4019 (2000).
[13] N. G. Green, A. Ramos, A. Gonzalez, H. Morgan, and A. Castellanos, Phys. Rev. E **66**, 026305 (2002).
[14] M. R. Bown and C. D. Meinhart, Microfluid. Nanofluid. **2**, 513 (2006).
[15] P. K. Wong, C.-Y. Chen, T.-H. Wang, and C.-M. Ho, Anal. Chem. **76**, 6908 (2004).
[16] M. Z. Bazant, K. Thornton, and A. Ajdari, Phys. Rev. E **70**, 021506 (2004).
[17] J. A. Levitan, S. Devasenathipathy, V. Studer, Y. Ben, T. Thorsen, T. M. Squires, and M. Z. Bazant, Colloids Surf., A **267**, 122 (2005).
[18] M. S. Kilic, M. Z. Bazant, and A. Ajdari, Phys. Rev. E **75**, 021503 (2007).
[19] K. T. Chu and M. Z. Bazant, Phys. Rev. E **74**, 011501 (2006).
[20] R. F. Probstein, *Physicochemical Hydrodynamics* (John Wiley & Sons, Hoboken, N.J., 2003).
[21] P. Sistat and G. Pourcelly, J. Electroanal. Chem. **460**, 53 (1999).
[22] Z. Yu and W. Admassu, Chem. Eng. Sci. **55**, 4629 (2000).

[23] I. Rubinstein and B. Zaltzman, Math. Models Meth. Appl. Sci. **11**, 263 (2001).

[24] I. Rubinstein and B. Zaltzman, Phys. Rev. E **72**, 011505 (2005).

[25] R. Q. Fu, T. W. Xu, W. H. Yang, and Z. X. Pan, Desalination **173**, 143 (2005).

[26] V. M. Volgin and A. D. Davydov, J. Membr. Sci. **259**, 110 (2005).

[27] S. J. Kim, Y.-C. Wang, J. H. Lee, H. Jang, and J. Han, Phys. Rev. Lett. **99**, 044501 (2007).

[28] R. B. Schoch, J. Han, and P. Renaud, Rev. Mod. Phys. **80**, 839 (2008).